Time-Dependent Deep Learning Manufacturing Process Model for Battery Electrode Microstructure Prediction

Diego E. Galvez-Aranda, Tan Le Dinh, Utkarsh Vijay, Franco M. Zanotto, and Alejandro A. Franco*

The manufacturing process of Lithium-ion battery electrodes directly affects the practical properties of the cells, such as their performance, durability, and safety. While computational physics-based modeling has been proven as a very useful method to produce insights on the manufacturing properties interdependencies as well as the formation of electrode microstructures, their high computational costs prevent their direct utilization in electrode optimization loops. In this work, a novel time-dependent deep learning (DL) model of the battery electrodes manufacturing process is reported, demonstrated for calendering of nickel manganese cobalt (NMC111) electrodes, and trained with time-series data arising from physics-based Discrete Element Method (DEM) simulations. The DL model predictions are validated by comparing evaluation metrics (e.g., mean square error (MSE) and R^2 score) and electrode functional metrics (contact surface area, porosity, diffusivity, and tortuosity factor), showing very good accuracy with respect to the DEM simulations. The DL model can remarkably capture the elastic recovery of the electrode upon compression (spring-back phenomenon) and the main 3D electrode microstructure features without using the functional descriptors for its training. Furthermore, the DL model has a significantly lower computational cost than the DEM simulations, paving the way toward quasi-real-time optimization loops of the 3D electrode architecture predicting the calendering conditions to adopt in order to obtain the desired electrode performance.

1. Introduction

Li-ion batteries (LIB) have been at the forefront of secondary energy storage devices, widely used as the main power source for electronic devices. The recent transition to Electric Vehicles (EVs) has further led to a surge in the demand for LIBs, thus, leading to a consequent increase in research, particularly focusing on the performance enhancement and the reduction of production cost of LIB cells. Among many studies being conducted, one such is the optimization of the electrode architecture or so-called electrode microstructure. Such microstructure, characterized by the spatial location of the active material (AM) particles, the carbon additives, the binder, and the pore network, determines the practical properties of the electrode and the cell, such as their energy density, power density, durability, and safety.[1–5] In turn, the electrode microstructure is determined by its manufacturing process.

The electrode manufacturing process widely followed by LIB cell manufacturers is a wet process, i.e., it requires the use of solvents. It can be decomposed overall in 3 stages (**Figure 1a**), one following the other: slurry preparation through mixing (from the suspension of the AM, carbon additive, and binder in the solvent) following a pre-mixing step, slurry coating (on a current collector) and drying, and calendering of the dried electrode. Each stage has a substantial impact on the electrode microstructure features.[6]

D. E. Galvez-Aranda, T. L. Dinh, U. Vijay, F. M. Zanotto, A. A. Franco
Laboratoire de Réactivité et Chimie des Solides (LRCS)
Université de Picardie Jules Verne
Hub de l'Energie, UMR CNRS 7314, 15 rue Baudelocque, Amiens 80039, France
E-mail: alejandro.franco@u-picardie.fr

D. E. Galvez-Aranda, T. L. Dinh, F. M. Zanotto, A. A. Franco
Réseau sur le Stockage Electrochimique de l'Energie (RS2E)
FR CNRS 3459
Hub de l'Energie
15 rue Baudelocque, Cedex, Amiens 80039, France

U. Vijay, A. A. Franco
ALISTORE-European Research Institute
FR CNRS 3104
Hub de l'Energie
15 rue Baudelocque, Cedex, Amiens 80039, France

A. A. Franco
Institut Universitaire de France
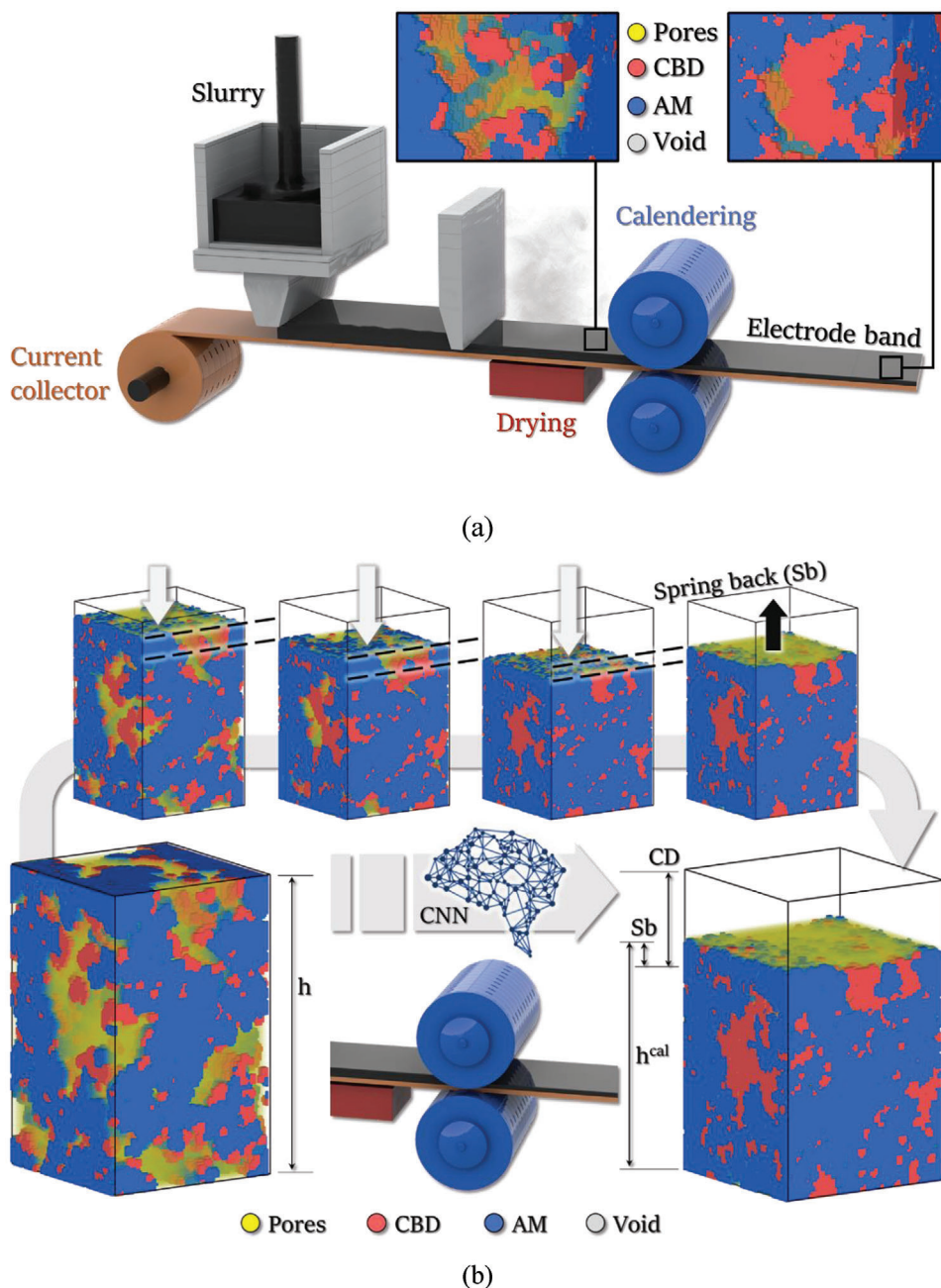103 Boulevard Saint Michel, Paris 75005, France

Figure 1. a) Diagram illustrating the initial stages of the manufacturing process of lithium-ion battery electrodes. b) Schematic representation of our deep-learning model for 3D electrode microstructure prediction during the calendering process. The approach allows to obtain a time series of the electrode microstructure evolution during its calendering and allows us to predict the final relaxation of it, all this as a function of the desired CD, which is used as an input of the model and in the real calendering process. Four phases are defined in the model: pores, CBD, AM, and void (region on top of the electrode). In the figure, h and h^{cal} refer to the uncalendered and calendered electrode thicknesses respectively.

Consequently, understanding the influence of each parameter at each manufacturing stage on the electrode architecture is crucial for optimizing the performance of LIB cells. The slurry stage, as the initial stage of the LIB manufacturing process, has an impact on the electrode coating microstructure, as well as the distribution of the binder and conductive additive, affecting its electronic and ionic resistances.[7] During the drying stage, electrode layer properties such as microstructure heterogeneities within

the electrode are highly dependent upon the solvent evaporation rate.[8] Furthermore, it is noted that the drying parameters are a significant factor in determining the electrode electrochemical properties.[9] About the calendering stage, it is used to reduce the microstructure porosity by utilizing a two-roll compactor reducing electrode thickness, and compressing it to reach a target density. This procedure alters several electrode properties, such as thickness, porosity, tortuosity factor, and adhesion of the

2400376 (2 of 13)

electrode to the current collector.[4] The calendering parameters, such as compression degree (CD), defined as the percentage of reduction in thickness with respect to the dried electrode, the temperature, the line load, and the roll speed have a significant impact on the electrode transport properties and wettability by the electrolyte.[10]

Besides experimental efforts to examine the impact of manufacturing parameters on electrode performance,[6,11] mesoscale computational modeling has arisen as a valuable complementary tool to study how manufacturing parameters impact the electrode microstructure. Several pioneering tools supported on this mesoscale modeling have been previously proposed by us, providing insights into the impact of manufacturing parameters on the cell electrochemical performance[12–14] and enabling the optimization of the fabrication process to diminish the manufacturing cost and the environmental effects. While slurry and drying stages are equally crucial to the final electrode microstructure, calendering has a more direct influence since it is the last stage.[15–16] Therefore, the study of the calendering process is important to understand the performance of the fabricated electrode. In that line, besides experimental efforts, computational methodologies have been proposed and used. Additionally, a computational approach allows researchers to investigate a wide diversity of electrode materials, compositions, initial thicknesses, and so on, without the need for physical experiments, saving resources, time, and reducing the risk of potential errors.[17] In the context of our ERC-funded ARTISTIC project initiative, we have demonstrated how innovative experimentally validated physics-based simulations of the manufacturing process, including calendering, are beneficial in understanding the complexity of the different manufacturing process steps and their interrelationships in order to fabricate optimized electrodes.[18,19,38]

During the calendering process, important properties and phenomena, such as elasticity, plasticity, and spring-back recovery, play a crucial role in directly influencing the final electrode performance. For example, due to applied stress, the electrode undergoes permanent (plastic deformation) and reversible (elastic deformation) changes affecting its porosity, density, and thickness.[20–22] Similar to plastic deformation, spring-back effects are also studied extensively from an experimental viewpoint to understand the relationship between the compaction process and performance in order to manufacture optimized electrodes.[23] In parallel to experimental studies, computational methods such as the Discrete Element Method (DEM) have been applied to understand calendering effects on final electrode properties.[10,15,24–26] Furthermore, the development of high-performance computing (HPC), for instance, supercomputers and cloud computing services, coupled with a sub-field of Artificial Intelligence (AI) such as Deep Learning (DL), are resources that can be used to accelerate the battery manufacturing process optimization as a whole.[25–26] For example, Shodiev et al., in our group, predicted electrolyte flow infiltration over time by using a multi-layer perceptron (MLP) approach.[27] Another study conducted by Duquesnoy et al. in our group developed a data-driven fast framework to forecast electrode slurries' rheological properties simulated by coarse-grained molecular dynamics.[28]

Similarly, Convolutional neural networks (CNNs) have emerged as a primarily DL approach when dealing with multidimensional data input, such as the ones arising from image processing, taking advantage of the handling of input data topology.[29] CNNs are made up of three major types of layers, namely convolutional layer, pooling layer, and fully-connected layer.[29] The convolutional layer comprises filters, also called kernels, used to capture the specific features from the input data. Thus, CNNs are built by stacking multiple convolutional layers to extract low-level to high-level patterns or features. Pooling layers, which usually come after convolutional layers, are used to decrease the data dimensions, thus reducing the computational cost. There are three main types of pooling layers: max, average, and mixed pooling,[30] and can be used depending on the requirement of the study. The fully connected layers are used to connect neurons between two different layers, as well as process the flattened features in order to implement the final tasks, for example, classification or regression problems. The number of neurons in fully connected layers depends on the complexity of the problem. CNN architecture follows a hierarchical structure, allowing the extraction of higher-level features obtaining lower-level ones by considering proximal spatial correlations. Therefore, CNN are suitable to deal with time-series datasets,[31] generally 1D grid topology, or imagery data sets which can be a 2D or 3D grid of pixels. Marcato et al. used, within our group, the results of a 3D-resolved heterogeneous electrochemical model to train a CNN, which is then used to simulate with 3D resolution, the spatio-temporal lithiation heterogeneities of an NMC111 electrode (in a half-cell configuration) as well as its corresponding galvanostatic discharge curve.[32]

In addition, CNN, when coupled with MLP or Long Short-Term Memory (LSTM), makes it possible to perform time-series forecasting, which is one of the bases of the study presented in this article. Such combinations also reduce the complexity of training a DL model.[31] As an example of 3D structure prediction, Pierson et al. employed a CNN-based model to predict the microstructure-sensitive evolution of 3D cracking paths in a polycrystalline alloy.[33] Additionally, Yang et al. present a DL approach combining CNN and LSTM to predict voltage discharge curves of 3D AM particle microstructures.[34] Besides time-series studies, another approach is the generation of 3D image data. For instance, Kench et al. developed a model using Generative adversarial networks (GANs) trained with tomography and/or Scanning Electron Microscopy images to generate static 3D samples given some microstructural metrics.[35] However, we believe that the development of a physics-informed model, like the one presented by us in this article, able to generate not only the final electrode microstructure but also to capture the particle rearrangement dynamics occurring during the whole manufacturing process, is necessary to optimize the influence of manufacturing parameters on the electrode architecture.

In the present work, we propose a novel DL model trained with a physics-informed dataset arising from electrode microstructures generated by physics-based manufacturing simulations (Figure 1b). Such dataset consists of 3D electrode microstructures with realistic active material (AM) particle shapes previously produced by us by utilizing a computational electrode manufacturing simulation workflow combining Coarse Grained Particle Dynamics (CGPD) (simulating the slurry and its drying) and DEM (simulating the calendering of the dried coating).[36] The data generated by this physics-based electrode manufacturing model is used to train a CNN and further optimize its ar-

ADVANCED
SCIENCE NEWS

www.advancedsciencenews.com

ADVANCED
ENERGY
MATERIALS

www.advenergymat.de

chitecture to predict the 3D electrode microstructure evolution over time during the calendering process. For validation, we employ purely data metrics as well as electrode functional metrics to compare predicted versus targeted microstructures. Such an approach of combining physics-based calendering simulation and DL (CNN), which is the focus of our study, and for the first time in the field of battery manufacturing, will give researchers an innovative and powerful tool to analyze complex electrode image data which can be generated synthetically, through simulations, or experimentally, through *in operando* tomography techniques. We demonstrate our DL model here as a proof-of-concept of the applicability of CNN for time-dependent physics problems. The presented DL model demonstrates a predictive accuracy evaluated by different metrics discussed in the following sections. Additionally, it allows to study of electrode functional parameters at different CD with much less computational cost (DL wall time is 15 s per step in comparison to the ≈47 min per step of the DEM model), keeping its accuracy and paving the way toward high-throughput screening of the influence of calendering conditions on electrode microstructure and its optimization. In the following sections, we discuss the methodology in detail followed by the results obtained and the conclusions of our study.

2. Experimental Section

2.1. Data Generation

To generate the data for training and testing, the physics-based computational electrode manufacturing simulation workflow was used, which was previously reported.[36] This workflow consists of the sequential linking of the CGPD approach, to simulate the slurry and its drying, and DEM, simulating the calendering of the resulting electrode. Details regarding the initial configuration, particle size distribution, and force field parameter values were listed in the supplementary information of our past work.[36] The CGPD/DEM workflow employed active material particle sizes and shapes obtained from Computer Tomography and was already validated by experiments showing good agreement in electrode functional metrics such as tortuosity factor and porosity.[36]

In the current work, the specific focus was on calendering step for one electrode formulation: 96% NMC111 – 2% C65 – 2% PVdF (96% AM and 4% carbon-binder domain -CBD- in the simulation). Four synthetic electrodes were prepared. For each electrode, seven CD values were simulated: 20%, 25%, 30%, 35%, 40%, 45%, and 50%, resulting in a total of 28 calendering simulations. Each simulation consists of a series of timeframes that capture the microstructure evolution over time during the calendering process. For the current work, the compression rate was kept constant, therefore the number of timeframes (steps) per CD value was 14, 18, 21, 24, 28, 31, and 35, corresponding to 20%, 25%, 30%, 35%, 40%, 45%, and 50% CD respectively. Each timeframe corresponded to 75 microseconds of simulation time.

2.2. Voxelization Technique

A 3D conversion technique was used to capture the NMC cathode geometrical shape under uniaxial compression at constant

speed modeled by the simulated data. The data was segmented into its various material phases and voxelized to rebuild the microstructure in a format that could be used with the CNN architecture presented in the current work. In order to achieve it, the voxelization algorithm was applied to extract particle positions to create the voxel grid. Specifically, the dimensions of the 3D space were represented using the size and resolution of the voxel grid. Each particle was placed into the corresponding voxel based on its spatial coordinates by discretizing the continuous space into voxel cells and determining which cell each particle falls into. After voxelization, the microstructure was composed of a grid of $76 \times 76 \times 125$ voxels. The dimension of a voxel was $0.4 \times 0.4 \times 0.4$ µm. Three different voxel values were generated to refer to a specific material from the original microstructure: 0 for pores, 1 for CBD, and 2 for AM. Additionally, a type 4 was created to refer to the void generated due to the calendering process. The Open Visualization Tool (OVITO)[37] package was used for the microstructure visualization.

2.3. Data Generation

Our 4D dataset (3D microstructures over time) was composed of 28 time series (TS). Every TS was a sequence of m frames, $S_n = [s_1, s_2, s_3, ..., s_{m-1}, s_m]$ where S_n is the nth TS ($n = 1 \rightarrow 28$), and s_m is the 3D voxelized microstructure ($76 \times 76 \times 125$ voxels) at frame m. A sliding window of 3 frames was prepared, dividing the total m frames into sets of observations based on the past 3 lags of S_n. As a result, the following matrix per TS was generated:

$$S_{[n]} = \begin{bmatrix} s_1 & s_2 & s_3 & s_4 \\ s_2 & s_3 & s_4 & s_5 \\ \vdots & \vdots & \vdots & \vdots \\ s_{m-4} & s_{m-3} & s_{m-2} & s_{m-1} \\ s_{m-3} & s_{m-2} & s_{m-1} & s_m \end{bmatrix} \quad (1)$$

$S_{[n]}$ contains the m frames divided in a sliding window of three frames, where $[n]$ is the corresponding n^{th} TS ($n = 1 \rightarrow 28$). The target values were given in the fourth column and their corresponding attributes or predictors were the previous 3 values listed from the first to third columns in the $S_{[n]}$ matrix. As an example, the past lags corresponding to the s_4 target value was $[s_1, s_2, s_3]$. Then, $S_{[n]}$ was divided into two matrices, $X_{[n]}$ containing the three past lags and $Y_{[n]}$ containing the target values.

Out of the 28 TS, 24 were taken for training and the remaining 4 for testing. Additionally, 20% of the training dataset was taken randomly as a validation dataset during model training. Therefore, the full dataset was divided into 4 matrices, X_{train}, Y_{train}, X_{test} and Y_{test}:

$$X_{train} = \begin{bmatrix} X_{[1]} \\ X_{[2]} \\ \vdots \\ X_{[23]} \\ X_{[24]} \end{bmatrix} \quad Y_{train} = \begin{bmatrix} Y_{[1]} \\ Y_{[2]} \\ \vdots \\ Y_{[23]} \\ Y_{[24]} \end{bmatrix} \quad X_{test} = \begin{bmatrix} X_{[25]} \\ X_{[26]} \\ X_{[27]} \\ X_{[28]} \end{bmatrix} \quad Y_{test} = \begin{bmatrix} Y_{[25]} \\ Y_{[26]} \\ Y_{[27]} \\ Y_{[28]} \end{bmatrix}$$

$$(2)$$

**ADVANCED
SCIENCE NEWS**

www.advancedsciencenews.com
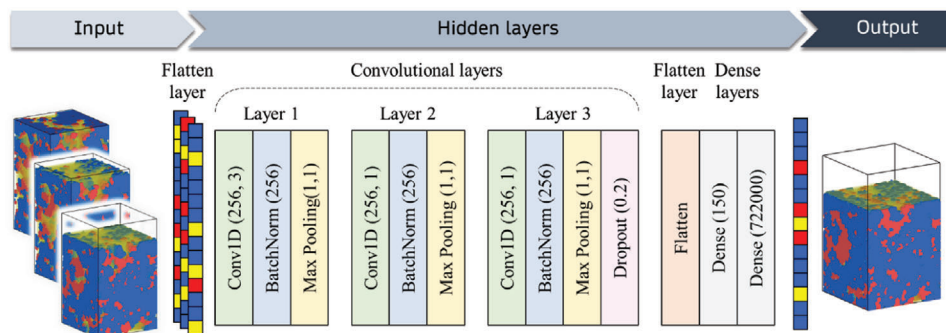
**ADVANCED
ENERGY
MATERIALS**

www.advenergymat.de

Figure 2. Architecture of the 1D-CNN employed for our time-series electrode calendering simulation. The network consists of the following layers: input layer, hidden layers (convolution, batch normalization, max-pooling, dropout layers, and fully connected layers), and output layer.

2.4. CNN Model

CNN has been widely used to develop DL models managing imagery datasets in several application fields,[33] being a suitable tool to work with pre-processed 3D voxelized datasets. In the present work, and for the first time to our knowledge in the field of battery manufacturing, the DL approach based on a 1D-CNN was used to learn about time-series data. The proposed 1D-CNN architecture to train the time series is depicted in **Figure 2**. For the approach, we take advantage of CNN image-processing method but apply the network to a very different set of 1D numeric arrays, even though the data dimension was originally a 3D voxelized data. Therefore, the original 3D voxelized data was re-shaped into a 1D numeric array for every time step (input layer). Through this re-shape, in terms of the local environment, voxels still represented correlated local features, adding that they can now be connected with consecutive time series.

The CNN architecture used in the current work was determined after an optimization process explained in the results and discussion section. The optimized CNN architecture was composed of an initial convolution layer using 256 filters and a kernel size of 3. Additionally, a batch normalization technique was added next to the convolution layer to make the output distribution more even, reaching training convergence faster.[39] Then, a max-pooling layer was adopted for a down spatial size sample of the output, reducing the computational complexity of the network. 1D max-pooling with a pooling size and stride size of 1 was used. The second convolution layer followed the same structure and logic explained in the first one. In the third convolution layer, a dropout technique was adopted to prevent overfitting and improve generalization during training.[40] The dropout rate was set to 0.2. Before feeding the fully connected layers with the extracted features a flattened layer was used. At the end, two fully connected layers were included obtaining a flattened 1-D array containing the predicted microstructure which was then re-shaped into a 3D matrix (output layer).

The model was optimized by minimizing a mean square error (MSE) cost function using the Adam,[41] optimizer since it was one of the most stable gradient descent optimizers.[42] The CNN model was implemented using the Python libraries Tensorflow[43] and Keras,[44] within the 3.9 version of Python. The data set was divided randomly into training (24) and testing datasets (4). An additional dataset was generated from DEM purely for testing purposes, consisting of 7 calendering degrees for the same initial microstructure. Then, the training dataset was divided randomly into training and validation in a ratio of 90 to 10, respectively. The validation set was used to monitor the convergence of the model during the training process. As opposed to the validation set, the test set was completely withheld from the training process. It was believed that the total data set composed of 28 simulations was good enough for CNN to learn recognized patterns when dealing with time-series data, as shown in our previous work dealing with 3D-resolved electrochemical simulation data.[32]

2.5. Evaluation Metrics

In this study, two different metrics approaches were used to evaluate the performance of the CNN model: data and electrode functional metrics. As data metrics, MSE, mean absolute error (MAE) and R^2 score were the validation data metrics chosen to evaluate the performance of the CNN model. During the training cycle, MSE was used as the overall loss function for evaluation. For testing, in addition to MSE, R^2 score was also calculated to evaluate the performance of the network. R^2 score was defined as:

$$R^2 = 1 - \frac{\sum_{k=1}^{N_k} \sum_{j=1}^{N_j} \sum_{i=1}^{N_i} \left(v_g(i,j,k) - v_p(i,j,k)\right)^2}{\sum_{k=1}^{N_k} \sum_{j=1}^{N_j} \sum_{i=1}^{N_i} \left(v_g(i,j,k) - \bar{v}\right)^2} \tag{3}$$

$$\bar{v} = \frac{\sum_{k=1}^{N_k} \sum_{j=1}^{N_j} \sum_{i=1}^{N_i} v_g(i,j,k)}{N_k N_j N_i} \tag{4}$$

where $v_g(i,j,k)$ and $v_p(i,j,k)$ were the voxel values of ground truth and predictions respectively, N_i, N_j and N_k were the total number of voxels on each axis and $\bar{v}$ is the average voxel value of ground truth. For our data, N_i, N_j and N_k were equal to 76, 76, and 125, respectively.

2.6. Electrode Functional Metrics

The ability of lithium ions to diffuse through the pore network of the structure is a crucial factor for the good performance of
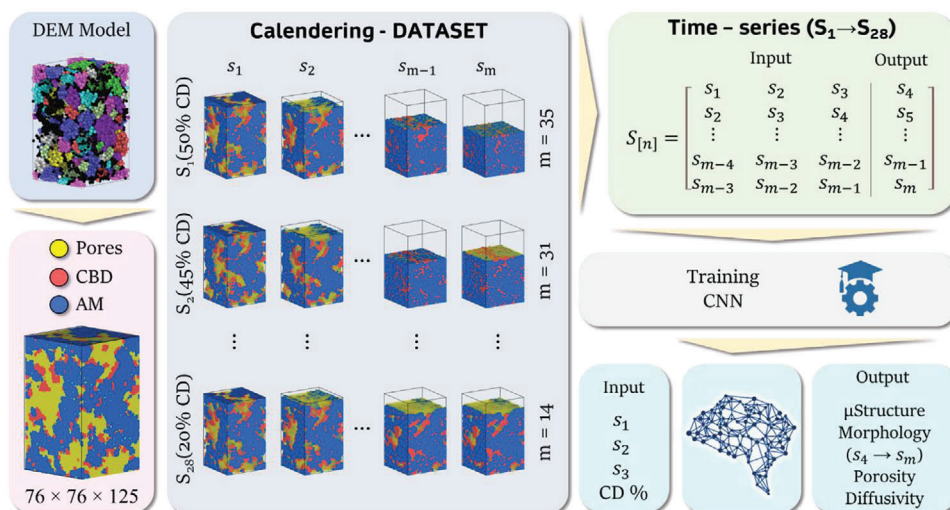
Figure 3. Schematic representation of the framework presented in the current work, starting from the 3D microstructure data reconstruction from DEM data, to train a CNN over a time series. After training, the model performance is assessed through evaluation and electrode functional metrics.

electrodes. Since it is highly dependent on the arrangement of the different phases along the electrode, characterizing it allowed comparing DL predictions versus DEM results in meaningful terms. In order to do this, stationary state diffusion calculations allowed to determine tortuosity factor and effective diffusivity values across the thickness of the electrode. Fick's laws were solved along the pore network, defining periodic boundary conditions on the outer planes in the x and y directions, and setting Li$^+$ concentration as 0 mM and 1 mM on the opposing outer planes in the z direction.

The effective diffusivity is obtained from the overall diffusive flux (J) as:

$$D_{eff} = -J \times length / 1\text{mM} \qquad (5)$$

where $length$ is the height of the simulation domain. Bulk diffusivity values of the pore and the CBD domains for the purposes of this calculation are taken from the work conducted by our group (Chouchane et al.) on NMC morphology and its performance.[45]

From the effective diffusivity value, and directly extracting the porosity of the system from the geometry, the tortuosity factor could be calculated according to the McMullin number [46]

$$\left(\tau = \frac{\sigma_{bulk}}{\sigma_{eff}} \times \varepsilon \right) \qquad (6)$$

where σ_{bulk} and σ_{eff} are the pore and effective ionic conductivities respectively, τ the electrode tortuosity factor, and ε the electrode porosity.

The diffusivity calculations were performed using the DiffuDict module in GeoDict 2023 (Math2Market).[45]

2.7. Framework

The presented framework started taking as input the 3D electrode microstructures preprocessed from the DEM data through a 3D voxelization technique. The full dataset, composed of 3D microstructures over time, was rearranged into a time-series format, being divided into input, 3 consecutive time samples, and output, the next time sample. Then, the CNN model was trained from this time-series dataset. After training, the CNN model provided output as the evolution in time of the 3D microstructure under the effects of a set CD. Then, the output of the model was evaluated through two kinds of metrics: one based on purely data comparison, and the other one comparing essential electrode functional properties such as porosity, diffusivity, and tortuosity factor, between the predicted and the DEM ground truth microstructures (**Figure 3**). For demonstration, the present work was focused on the study of a constant compression speed component application (top to bottom – z-axis) over different CDs.

3. Results and Discussion

3.1. CNN Optimization

Hyperparameters control the learning process of a machine learning model. It is, therefore, crucial to fine-tune them to get the best CNN architecture. Nevertheless, tuning hyperparameters is one of the most tedious tasks in machine learning projects. Thus, we wrote an optimization algorithm, using Optuna[47] package, to tune the different hyperparameters, namely activation function, dropout, number of convolution, and full-connected layers to obtain the best performance for our DL model. The optimization process using Optuna is comprised of a set of trials, where a trial is a single execution of the objective function with a specific list of hyperparameters. The objective function is defined by the users to evaluate the performance of the model based on the given hyperparameters in the search space. The objective function will return the training or validation score depending on our requirements. Optuna, then, aims to minimize or maximize the objective function. In particular, the mean squared error is minimized in our study. Over 500 trials have been implemented on the MatriCS HPC platform of our

ADVANCED
SCIENCE NEWS

www.advancedsciencenews.com

ADVANCED
ENERGY
MATERIALS

www.advenergymat.de

Table 1. Summary of some of the different CNN architectures explored in the present work with their corresponding MSE for training and validation sets.

Models	Convolutional layers	Fully connected layers	Dropout	MSE – training	MSE – validation
A	2 – LeakyReLU	2 – tanh	0.372	0.1681	0.1348
B	3 – mish	2 – LeakyReLU	0.364	0.1176	0.1312
C	3 – mish	2 – mish	0.200	0.0357	0.0257
D	3 – relu	2 – relu	0.200	0.0088	0.0085

Universite de Picardie Jules Verne. We divide the optimization process into two stages. In the first stage, the number of convolutional and deep layers is optimized. In the second stage, the CNN architecture obtained in the first stage is tested with different activation functions (**Table** 1). This two-stage approach is performed to decrease the computational cost during the optimization. All models run during 1000 epochs using Adam optimizers. Model D shows the best score in terms of MSE compared to others. Specifically, MSE on the training data set is ≈0.0088 while MSE on the validation set is approximately 0.0085, indicating no overfitting in the model. Model D architecture is the one used in the current work and is shown in Figure 2. Further details regarding the Model D architecture are also shown in Table S1 (Supporting Information).

Figure 4 shows the evolution of both loss functions, MSE and MAE as a function of the epochs. In Model D, it is observed that MSE and MAE decrease smoothly for both training and validation data, demonstrating that the parameters of the models converge to optimal values without overfitting. This is concluded by the negligible difference between the training and validation losses. Similarly, there is convergence in MAE values, which after 1000 epochs are 0.0689 and 0.0662, for training and validation datasets, respectively. MSE values are listed in Table 1.

3.2. Model Evaluation By Data Metrics

The testing dataset consists of 11 TS taken from four different initial microstructure configurations. **Table** 2 indicates how the 11 testing TS are distributed considering the 4 initial electrode microstructures. For example, for microstructure I, DEM simulations at 20%, 25%, 30%, 35%, 40%, and 50% CD are used in the training dataset leaving the 45% CD for testing. For microstructure II, DEM simulations at 20%, 25%, 30%, 40%, 45%, and 50%

CD are used in the training dataset leaving the 35% CD for testing. For microstructure III, DEM simulations at 20%, 30%, 35%, 40%, and 50% CD are used in the training dataset leaving the 25% and 45% CD for testing. Finally, for microstructure IV, no DEM simulation is considered in the training data set, therefore, all the CD simulations are used for testing.

To verify that the time-dependent DL calendering model can capture the effects on the microstructure properties, we evaluated the different DL-predicted TS versus their corresponding DEM-produced microstructures. The microstructural comparison is performed in two ways: volume (given by number of voxel units) evolution and R^2 score over the whole time frame. For microstructure I, at 45% CD, it is observed that the calendering DL model can capture the spring-back phenomena (partial elastic recovery of the electrode) which occurs when the calendering roll (represented in the DEM model as a planar press) is released once the desired CD is reached (**Figure** 5a). The R^2 score indicates how similar are the two microstructures, the DL-predicted one versus the DEM-target one. For microstructure I, it is observed that the R^2 score is always above 90% at all time frames, indicating that the DL-predicted microstructures over time are very similar to their corresponding DEM-target ones (Figure 5b,c).

Table 2. Summary of testing data used to study our DL model performance.

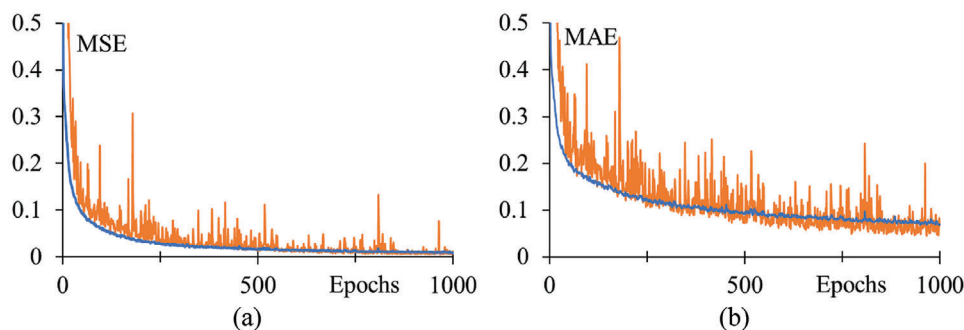| Microstructure	% CD of training data	% CD of testing data
I	20 – 25 – 30 – 35 – 40 – 50	45
II	20 – 25 – 30 – 40 – 45 – 50	35
III	20 – 30 – 35 – 40 – 50	25 – 45
IV		20 – 25 – 30 – 35 – 40 – 45 – 50

Figure 4. Graph of loss, a) MSE and b) MAE, for training and validation datasets using model D during the network training. Blue and orange curves refer to training and validation sets, respectively.
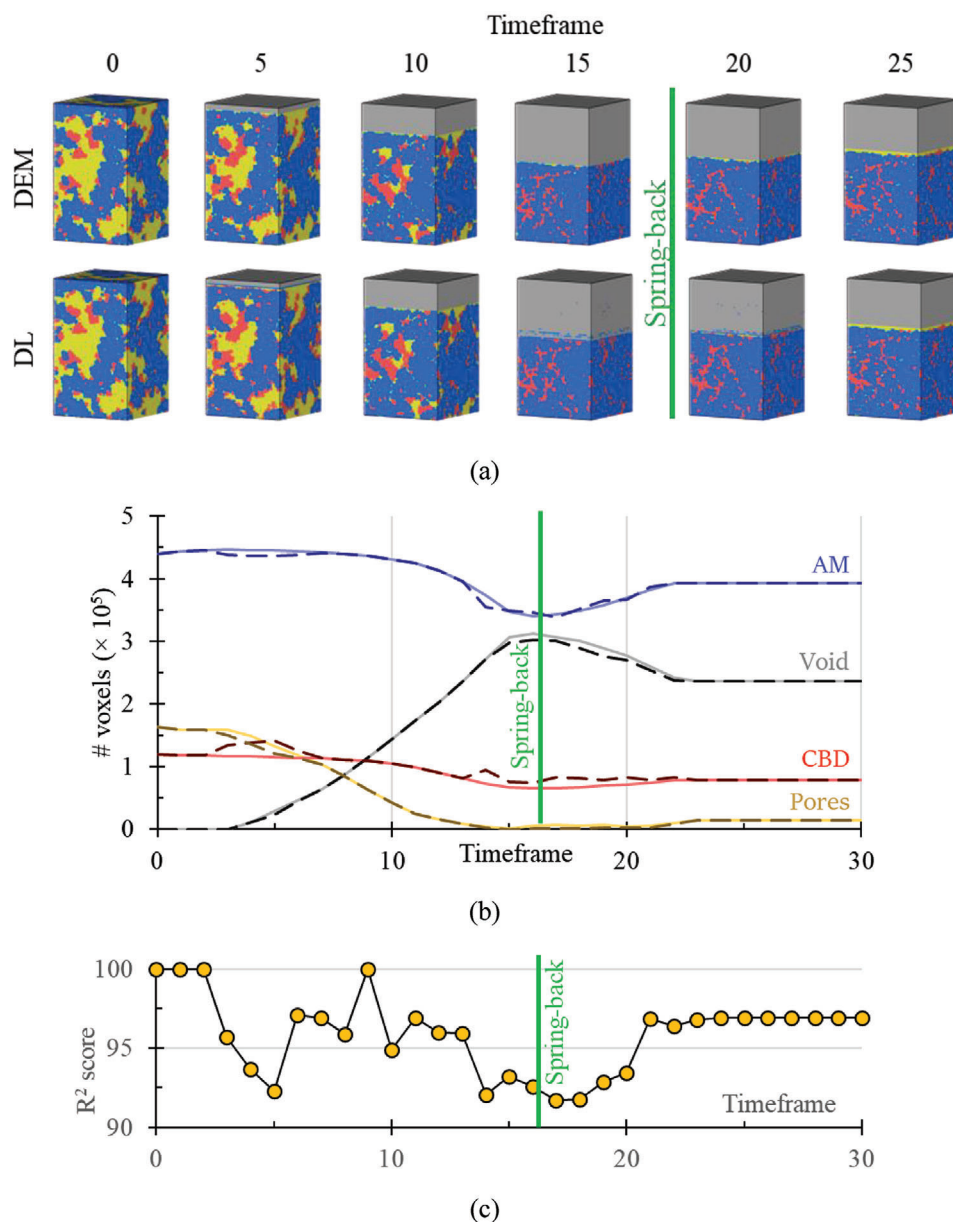
Figure 5. a) DEM target microstructures over time versus DL-predicted microstructures over time. b) Evolution of the volume of the four different phases (AM, CBD, Pores & Void) in number of voxels (# voxels) units versus time of the testing data, Microstructure I at a 45% CD. c) R^2 score comparing DEM target versus DL predicted over time.

Similarly, we calculate the volume evolution and R^2 score over the whole-time lapse for microstructure II at 35% CD (**Figure 6**a,b) and for microstructure III at 25% CD (Figure 6c,d) and 45% CD (Figure 6e,f). As it is shown for the microstructure I at 45% CD, on the volume evolution, it can be observed that the DL model accurately predicts the spring-back phenomena occurring at 25% and 35% CD, following the trend of the DEM target evolution at the different CD. Additionally, the R^2 score along the different microstructures is on average ≈95% over the whole-time lapse, indicating that the DL-predicted microstructure is remarkably similar to its corresponding DEM-targeted one. Videos of the DEM versus DL microstructure evolution

during calendering are available in the supporting information section.

3.3. Model Evaluation By Electrode Functional Metrics

We also quantify the contact surface (voxel²) between the three phases: Pore – CBD, Pore – AM, and AM – CBD. In **Table 3**, we compare the contact surface area obtained from our DL model versus the DEM model. Additionally, we calculate the relative error of the three contact surfaces. Figure S1 (Supporting Information) shows the different phases of evolution over time for Mi-
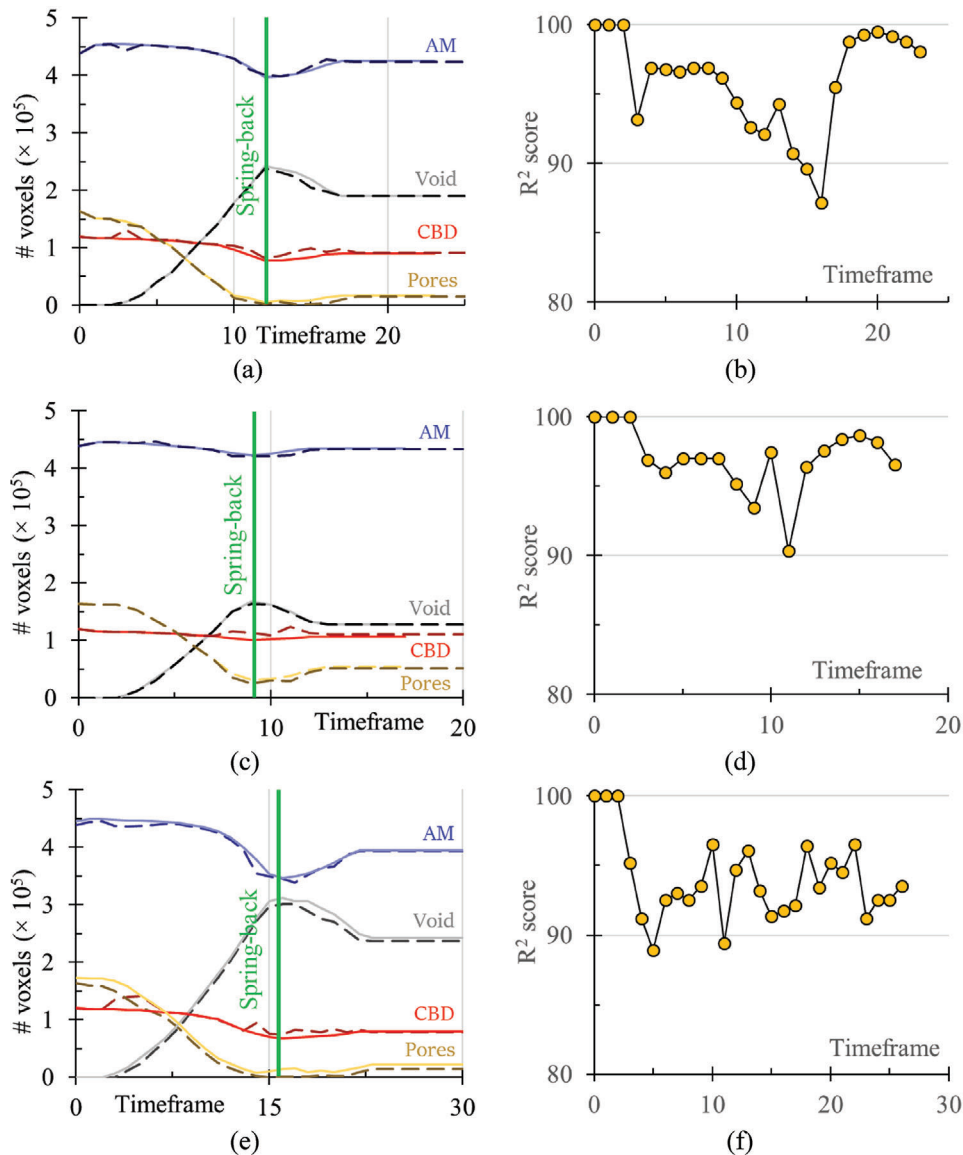
Figure 6. Evolution of the volume of the 4 different phases (AM, CBD, Pores & Void) in number of voxels (# voxels) units versus time of the testing data, microstructure II at a) 35% CD and microstructure III at c) 25% and e) 45% CD. R^2 score comparing DEM target versus DL predicted over time of the testing data, microstructure II at b) 35% CD and microstructure III at d) 25% and f) 45% CD.

Table 3. Contact surface area between the three phases: Pore, CBD, and AM. Surface units are given in voxel$^{.2}$

| | Microstructure I | | Microstructure II | | Microstructure III | | | |
| | 45% CD | | 35% CD | | 25% CD | | 45% CD | |
	DEM	DL	DEM	DL	DEM	DL	DEM	DL
Pore – CBD	4869	5259	5154	6018	20 763	23 717	5110	5930
Pore – AM	13 306	13 813	26 078	22 671	53 830	46 848	17 886	15 678
AM – CBD	134 879	143 851	126 960	131 843	96 311	112 326	149 154	162 341
Pore – CBD (error %)	8.01		16.76		14.23		16.05	
Pore – AM (error %)	3.81		13.06		12.97		12.34	
AM – CBD (error %)	6.65		3.85		16.63		8.84	

**ADVANCED
SCIENCE NEWS**

www.advancedsciencenews.com
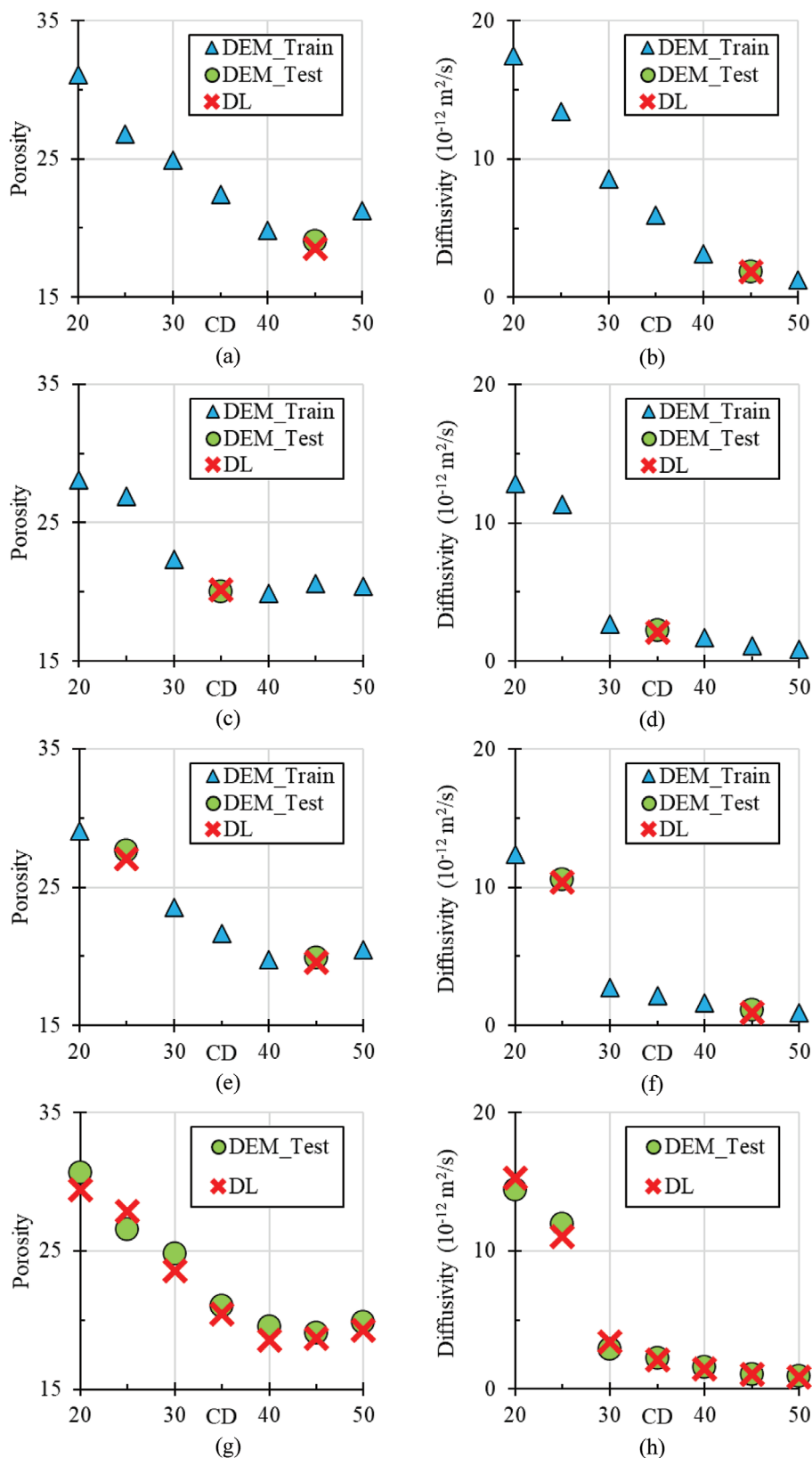
**ADVANCED
ENERGY
MATERIALS**

www.advenergymat.de

Figure 7. Calculated porosity of DEM training data (blue triangles) versus DEM testing data (green circles) versus DL predicted data (red crosses) of microstructure a) I, c) II, e) III, and g) IV. Diffusivity of DEM training data (blue triangles) versus DEM testing data (green circles) versus DL predicted data (red crosses) of microstructure b) I, d) II, f) III, and h) IV.

**ADVANCED
SCIENCE NEWS**

www.advancedsciencenews.com

**ADVANCED
ENERGY
MATERIALS**

www.advenergymat.de

crostructure III at 25% CD. It is observed that, on average, the error % of the AM – CBD contact surface is the smallest between the different phases, with a value of 8.99%. The average error % of the other two contact surfaces are 13.76% and 10.54% for Pore – CBD and Pore – AM respectively. From a purely data point of view, an average contact surface area error % of around or below 10% indicates that our model is predicting in an accurate way the geometrical arrangement between the phases. However, since the contact surface area is only one of the properties affecting the electrode electrochemical performance (e.g., controlling for instance the intercalation/de-intercalation kinetics of lithium ions, and the electronic charge transfer between AM and CBD),[24] we need to go beyond by also using other electrode functional metrics.

Even though an explicit structure-property linkage is not included in the DL model, the calculation of additional electrode functional properties such as porosity, diffusivity, and tortuosity factor, are crucial for characterizing and comprehending the structural conformation of a microstructure. In this approach, the listed properties are also used as metrics to compare the similarity of the DL-predicted microstructures versus the DEM-targeted ones. Numerical calculations of the three properties, porosity, diffusivity, and tortuosity factor, are determined according to the method described in the methodology section and results are shown in **Figure 7**.

For the four microstructures used for testing, I – II – III – IV, the DL model achieves an accurate prediction for both porosity and diffusivity. The relative error between the DL prediction and DEM testing data oscillates in the order of 0.5% – 9.8% for the four microstructures, indicating a reliable capacity of the DL model to predict unknown electrode functional properties. Thus, it can be concluded that the proposed DL model is also able to accurately predict the porosity and diffusivity of a calendered microstructure. In all four microstructure cases, porosity decreases as the CD goes up to 40%. Beyond 40% CD, the trend is not uniform, porosity fluctuates with an amplitude of ± 2%. Therefore, we consider that between 40 to 50% CD, the electrode has reached its mechanical limit to be compressed, and due to its spring-back phenomenon and initial electrode configuration, porosity does not follow a uniform trend. A porosity limit of ≈20% agrees with experimental reports which mention the challenge of going under it due to the fracture of secondary NMC particles.[15,48–49] Regarding the diffusivity, it decreases as the CD increases on both DEM and DL models. It is observed that the major drop in diffusivity occurs between 20 to 30% CD. Beyond 30% CD, changes in diffusivity are not that abrupt since the electrode is reaching its mechanical limit to be compressed. Therefore, structural changes and arrangements are not as radical as during 20 to 30% CD. Tortuosity factor values are reported in Table S2 (Supporting Information), together with the porosity and diffusivity values shown in Figure 7. It is observed that the tortuosity factor increases as CD increases, decreasing its efficiency to transport Li$^+$ as observed on the diffusivity values. The DL model predicted tortuosity factor values have an error of ± 5% with respect to the DEM model ones. In addition, both models present maximum porosity and lowest tortuosity factor for the uncalendered electrode. The observed general trend is, during calendering and as the CD increases, the porosity and tortuosity factors decrease and rise respectively. Considering potential un-

derestimation in experiments due to the difficulty in determining the CBD distribution and variability according to the tortuosity factor calculation method, results in Figure S2 (Supporting Information) should be seen as such, particularly for high CD.[36] While an eventual overestimation of tortuosity factor values can be attributed to the assumptions behind the Fickean diffusion-like method used for the calculation of the tortuosity factor from the 3D microstructure, this work aims to reproduce results from DEM with faster ML techniques. In this sense, the comparison shows remarkable agreement between the two microstructure generation techniques.

While this can be attributed to the assumptions of the DEM model, this work aims to reproduce results from DEM. Furthermore, the voxelization step makes our approach general enough to be trained on any microstructure simulations (or even experimental) results, ensuring its applicability as the state-of-the-art advances.

4. Conclusions and Perspectives

The innovative DL model presented in this work can predict an electrode microstructure evolution over time at a given compression degree during calendering and provide the associated final relaxed electrode microstructure. Here we used the formulation of 96% AM and 4% CBD as a proof of concept. The predictive performance of our DL model is evaluated by two types of metrics: one purely based on data, MSE, R^2 score, and contact surface between phases, and the second one based on functional properties such as porosity, diffusivity, and tortuosity. Using those two types of metrics together we observe that the DL model is able to predict the electrode microstructure evolution over time with remarkable accuracy. Furthermore, the DL model is able to replicate very accurately the spring-back phenomenon, occurring at different CDs. Regarding the computational cost, the DL model performs a timestep in 15 seconds (wall time). On the other hand, the DEM model performs an equivalent timestep in ∼ 47 minutes (wall time). Therefore, the DL model has tremendously decreased the computational cost of the simulation while keeping a high accuracy as demonstrated by the metrics result.

The number of timeframes extracted from the simulations and employed for training is a hyperparameter to be further investigated to evaluate its impact on the accuracy of the predictions. Grid resolution can also be considered as another hyperparameter that will affect the model performance. In the current work, we use a 76 × 76 × 125 voxel^3 resolution, resulting in a voxel size of 0.4 micrometer, which is almost four times smaller than the smallest particle in the DEM simulations. However, further exploration might be insightful as larger voxel sizes could provide faster results, but the accuracy of the model can be compromised. Finally, even though the DL model presented in the current work is trained for a specific formulation, transfer learning can be used to train a new DL model with predictive capabilities for other formulations, or even different electrode materials such as graphite, LFP, or blends. In that sense, more training datasets need to be generated and validated prior to the development of the DL model, and this is ongoing work in our group. Furthermore, the nature of the data set, which is a voxelized geometry, makes our approach general. Particularly, it would be interesting

**ADVANCED
SCIENCE NEWS**

www.advancedsciencenews.com

**ADVANCED
ENERGY
MATERIALS**

www.advenergymat.de

to adapt it to time series datasets obtained from 4D-computer tomography. For this reason, we are working on a model demonstration of the applicability of our method to tomography images with time series.

We believe that the speed and accuracy of the presented physics-informed DL model pave the way toward optimization loops of the electrode microstructure, by accounting explicitly for the 3D microstructural features (dealing with electrochemical and transport heterogeneities upon the electrode operation) and not only for the average properties of such electrodes as in our previous works.[50–51] Given the high accuracy of the DL model to predict calendered electrode microstructures with correct tortuosity factor and porosity values, and since those two properties have a high impact on the effective transport properties of Li^+ in the electrolyte, we can conclude that the model is also able to predict correctly the effect of the calendering on the transport properties. Regarding model limitations, we can observe that the error (target versus prediction) regarding the contact surface between phases varies around 10 to 15%, but when the overall electrode functional metrics are calculated, the error is less than 5%. Therefore, even though the overall electrode property presents high accuracy, the interfaces between phases can still be improved. This can be done by decreasing the voxel size: however, this will increase the computational cost during training. Additionally, we believe that using an input compression degree out of the range between 20 to 50 % CD might produce unphysical behaviors, therefore the model might not be suitable for extrapolation. Exploring extrapolation features will be part of our future work.

As shown in this work, our model can understand and predict the dynamics of the calendering process. Moreover, we consider that our model has tremendous potential to grow in several aspects such as accuracy and predictability. Therefore, our incoming efforts will be focused on continuing the development of the model and testing it for other formulations and in other manufacturing stages.

Supporting Information

Supporting Information is available from the Wiley Online Library or from the author.

Conflict of Interest

The authors declare no conflict of interest.

Author Contributions

D.E.G.-A.: Conceptualization; Methodology; Formal analysis; Investigation; Visualization: Writing original draft. T.L.D.: Formal analysis; Investigation; Writing original draft. U.V.: Formal analysis; Investigation; Writing original draft. F.M.Z.: Formal analysis; Investigation; Writing original draft. A.A.F.: Conceptualization; Methodology; Funding acquisition; Supervision; Resources; Writing original draft; Writing review & editing.

Data Availability Statement

Research data are not shared.

[1] J. Li, Z. Du, R. E. Ruther, S. J. An, L. A. David, K. Hays, M. Wood, N. D. Phillip, Y. Sheng, C. Mao, *Jom* **2017**, *69*, 1484.

[2] J. Xu, X. Cai, S. Cai, Y. Shao, C. Hu, S. Lu, S. Ding, *Energ. Environm. Mater.* **2023**, *6*, e12450.

[3] M. W. Nazar, N. Iqbal, M. Ali, H. Nazir, M. Z. B. Amjad, *J. Energy Storage* **2023**, *61*, 106800.

[4] R. Gonçalves, S. Lanceros-Méndez, C. Costa, *Electrochem. Commun.* **2022**, *135*, 107210.

[5] W. Mei, H. Chen, J. Sun, Q. Wang, *Sustain. Energ. Fuels* **2019**, *3*, 148.

[6] Z. Wang, C. Dai, K. Chen, Y. Wang, Q. Liu, Y. Liu, B. Ma, L. Mi, W. Mao, *J. Power Sources* **2022**, *551*, 232176.

[7] D. Grießl, A. Adam, K. Huber, A. Kwade, *J. Electrochem. Soc.* **2022**, *169*, 020531.

[8] M. Baunach, S. Jaiser, S. Schmelzle, H. Nirschl, P. Scharfer, W. Schabel, *Drying Technol.* **2016**, *34*, 462.

[9] Y. S. Zhang, N. E. Courtier, Z. Zhang, K. Liu, J. J. Bailey, A. M. Boyce, G. Richardson, P. R. Shearing, E. Kendrick, D. J. Brett, *Adv. Energy Mater.* **2022**, *12*, 2102233.

[10] M. Abdollahifar, H. Cavers, S. Scheffler, A. Diener, M. Lippke, A. Kwade, *Adv. Energy Mater.* **2023**, *13*, 2300973.

[11] L. S. Kremer, A. Hoffmann, T. Danner, S. Hein, B. Prifling, D. Westhoff, C. Dreer, A. Latz, V. Schmidt, M. Wohlfahrt-Mehrens, *Energy Technol.* **2020**, *8*, 1900167.

[12] T. Lombardo, J. B. Hoock, E. N. Primo, A. C. Ngandjong, M. Duquesnoy, A. A. Franco, *Batteries Supercaps* **2020**, *3*, 721.

[13] T. Lombardo, F. Caro, A. C. Ngandjong, J.-B. Hoock, M. Duquesnoy, J. C. Delepine, A. Ponchelet, S. Doison, A. A. Franco, *Batteries & Supercaps* **2022**, *5*, 202100324.

**ADVANCED
SCIENCE NEWS**

www.advancedsciencenews.com

**ADVANCED
ENERGY
MATERIALS**

www.advenergymat.de

[14] A. Shodiev, F. M. Zanotto, J. Yu, M. Chouchane, J. Li, A. A. Franco, *Energy Storage Mater.* **2022**, *49*, 268.

[15] J. Xu, B. Paredes-Goyes, Z. Su, M. Scheel, T. Weitkamp, A. Demortière, A. A. Franco, *Batteries Supercaps* **2023**, *6*, 12, 202300371.

[16] S. Scheffler, R. Jagau, N. Müller, A. Diener, A. Kwade, *Batteries* **2022**, *8*, 46.

[17] F. M. Zanotto, D. Z. Dominguez, E. Ayerbe, I. Boyano, C. Burmeister, M. Duquesnoy, M. Eisentraeger, J. F. Montaño, A. Gallo-Bueno, L. Gold, F. Hall, N. Kaden, B. Muerkens, L. Otaegui, Y. Reynier, S. Stier, M. Thomitzek, A. Turetskyy, N. Vallin, A. A. Franco, *Batteries - Supercaps* **2022**, *5*, 202200224.

[18] M. Alabdali, F. M. Zanotto, M. Duquesnoy, A. K. Hatz, D. Ma, J. Auvergniot, V. Viallet, V. Seznec, A. A. Franco, *J. Power Sources* **2023**, *580*, 233427.

[19] M. Chouchane, A. Rucci, T. Lombardo, A. C. Ngandjong, A. A. Franco, *J. Power Sources* **2019**, *444*, 227285.

[20] H. Liu, X. Cheng, Y. Chong, H. Yuan, J. Q. Huang, Q. Zhang, *Particuology* **2021**, *57*, 56.

[21] E. N. Primo, M. Touzin, A. A. Franco, *Batteries & Supercaps* **2021**, *4*, 834.

[22] E. N. Primo, M. Chouchane, M. Touzin, P. Vazquez, A. A. Franco, *J. Power Sources* **2021**, *488*, 229361.

[23] A. Diener, S. Ivanov, W. Haselrieder, A. Kwade, *Energy Technol.* **2022**, *10*, 2101033.

[24] C. Liu, T. Lombardo, J. Xu, A. C. Ngandjong, A. A. Franco, *Energy Storage Mater.* **2023**, *54*, 156.

[25] A. C. Ngandjong, T. Lombardo, E. N. Primo, M. Chouchane, A. Shodiev, O. Arcelus, A. A. Franco, *J. Power Sources* **2021**, *485*, 229320.

[26] M. Duquesnoy, T. Lombardo, M. Chouchane, E. N. Primo, A. A. Franco, *J. Power Sources* **2020**, *480*, 229103.

[27] A. Shodiev, M. Duquesnoy, O. Arcelus, M. Chouchane, J. Li, A. A. Franco, *J. Power Sources* **2021**, *511*, 230384.

[28] M. Duquesnoy, T. Lombardo, F. Caro, F. Haudiquez, A. C. Ngandjong, J. Xu, H. Oularbi, A. A. Franco, *npj Computat. Mater.* **2022**, *8*, 161.

[29] L. Alzubaidi, J. Zhang, A. J. Humaidi, A. Al-Dujaili, Y. Duan, O. Al-Shamma, J. Santamaría, M. A. Fadhel, M. Al-Amidie, L. Farhan, *J. Big Data* **2021**, *8*, 53.

[30] D. Yu, H. Wang, P. Chen, Z. Wei, *Rough Sets and Knowledge Technology* **2014**, 364.

[31] J. Brownlee, *Machine Learning Mastery* **2018**, 23.

[32] A. Marcato, J. E. Santos, C. Liu, G. Boccardo, D. Marchisio, A. A. Franco, *Energy Storage Mater.* **2023**, *63*, 102927.

[33] K. Pierson, A. Rahman, A. D. Spear, *Jom* **2019**, *71*, 2680.

[34] W. Yang, X. Yao, Z. Wang, P. Liu, H. Yan, Y. Xiao, K. Tantratian, W. Cai, L. Chen, *J. Power Sources* **2023**, *579*, 233087.

[35] S. Kench, S. J. Cooper, *Nat. Mach. Intell.* **2021**, *3*, 299.

[36] J. Xu, A. C. Ngandjong, C. Liu, F. M. Zanotto, O. Arcelus, A. Demortière, A. A. Franco, *J. Power Sources* **2023**, *554*, 232294.

[37] A. Stukowski, *Modell. Simul. Mater. Sci. Eng.* **2010**, *18*, 015012.

[38] T. Lombardo, F. Lambert, R. Russo, F. M. Zanotto, C. Frayret, G. Toussaint, P. Stevens, M. Becuwe, A. A. Franco, *Batteries Supercaps* **2022**, *5*, 202200116.

[39] S. Ioffe, C. Szegedy, in *Proceed. 32nd Int. Conf. Int. Conf. Mach. Learning*, *37*, Lille, France **2015**.

[40] N. Srivastava, G. Hinton, A. Krizhevsky, I. Sutskever, R. Salakhutdinov, *J. Mach. Learning Res.* **2014**, *15*, 1929.

[41] D. P. Kingma, J. Ba, arXiv preprint *arXiv:1412.6980* **2014**.

[42] S. Ruder, arXiv preprint *arXiv:1609.04747* **2016**.

[43] M. Abadi, P. Barham, J. Chen, Z. Chen, A. Davis, J. Dean, M. Devin, S. Ghemawat, G. Irving, M. Isard, presented at 12th USENIX *Symp. Operat. Syst. Design Implement.* (OSDI 16), **2016**.

[44] A. Kapoor, A. Gulli, S. Pal, F. Chollet, *Deep Learning with TensorFlow and Keras: Build and deploy supervised, unsupervised, deep, and reinforcement learning models*, Packt Publishing Ltd, UK **2022**.

[45] M. Chouchane, A. A. Franco, *Energy Storage Mater.* **2022**, *47*, 649.

[46] R. B. MacMullin, G. A. Muccini, *AIChE J.* **1956**, *2*, 393.

[47] T. Akiba, S. Sano, T. Yanase, T. Ohta, M. Koyama, presented at Proceed. 25th ACM SIGKDD Int. Conf. Knowled. Discov. Data Mining, Anchorage, AK, USA **2019**.

[48] R. Tao, B. Steinhoff, K. Uzun, B. La Riviere, K. Sardo, B. Skelly, R. Hill, Y. T. Cheng, J. Li, *J. Power Sources* **2023**, *581*, 233481.

[49] R. Xu, L. S. de Vasconcelos, J. Shi, J. Li, K. Zhao, *Experiment. Mechan.* **2018**, *58*, 549.

[50] M. Duquesnoy, C. Liu, D. Z. Dominguez, V. Kumar, E. Ayerbe, A. A. Franco, *Energy Storage Mater.* **2023**, *56*, 50.

[51] M. Duquesnoy, C. Liu, V. Kumar, E. Ayerbe, A. A. Franco, *J. Power Sources* **2024**, *590*, 233674.